Journal of Volcanology and Geothermal Research 354 (2018) 29–38

Contents lists available at ScienceDirect

Journal of Volcanology and Geothermal Research

journal homepage: www.elsevier.com/locate/jvolgeores

Permeability of volcanic rocks to gas and water

M.J. Heap *, T. Reuschlé, J.I. Farquharson, P. Baud

Géophysique Expérimentale, Institut de Physique de Globe de Strasbourg (UMR 7516 CNRS, Université de Strasbourg/EOST), 5 rue René Descartes, 67084 Strasbourg cedex, France

ARTICLE INFO

Article history:
Received 15 November 2017
Received in revised form 1 February 2018
Accepted 5 February 2018
Available online 6 February 2018

Keywords:
Permeability
Klinkenberg
Volcano
Pore fluid
Microstructure

ABSTRACT

The phase (gas or liquid) of the fluids within a porous volcanic system varies in both time and space. Laboratory experiments have shown that gas and water permeabilities can differ for the same rock sample, but experiments are biased towards rocks that contain minerals that are expected react with the pore fluid (such as the reaction between liquid water and clay). We present here the first study that systematically compares the gas and water permeability of volcanic rocks. Our data show that permeabilities to argon gas and deionised water can differ by a factor between two and five in two volcanic rocks (basalt and andesite) over a confining pressure range from 2 to 50 MPa. We suggest here that the microstructural elements that offer the shortest route through the sample—estimated to have an average radius ~0.1–0.5 μm using the Klinkenberg slip factor—are accessible to gas, but restricted or inaccessible to water. We speculate that water adsorption on the surface of these thin microstructural elements, assumed here to be tortuous/rough microcracks, reduces their effective radius and/or prevents access. These data have important implications for fluid flow and therefore the distribution and build-up of pore pressure within volcanic systems.

1. Introduction

Permeability is a measure of the ability of a material to transmit fluids [Guéguen and Palciauskas, 1994]. The permeability of volcanic rocks therefore largely controls the movement of fluids and the distribution of pore pressure in a volcanic edifice. The build-up of pore pressure within a volcanic system is thought to promote explosive volcanism [e.g., Eichelberger et al., 1986; Sparks, 1997; Melnik et al., 2005; Farquharson et al., 2017] and flank collapse [e.g., Reid, 2004] and, as such, many experimental and theoretical studies have been devoted to better understanding the permeability of volcanic materials [e.g., Eichelberger et al., 1986; Saar and Manga, 1999; Blower, 2001; Rust and Cashman, 2004; Mueller et al., 2005; Costa, 2006; Mueller et al., 2008; Wright et al., 2009; Degruyter et al., 2010; Lavallée et al., 2013; Gaunt et al., 2014; Farquharson et al., 2015, 2016; Heap and Kennedy, 2016; Wadsworth et al., 2016; Lindoo et al., 2016; Heap et al., 2016, 2017; Burgisser et al., 2017; Kushnir et al., 2017a; Colombier et al., 2017; Vasseur and Wadsworth, 2017; Kushnir et al., 2017b]. These studies, and many others, have shown that the permeability of volcanic materials is not only an increasing function of porosity (a scalar), but also highlight the importance of a wealth of additional parameters, such as porosity type (pores and microcracks), pore geometry (size, shape, and preferred orientation), porosity connectivity, and alteration, amongst others.

The constitutive equation that describes fluid flow through a porous medium is Darcy's law [Darcy, 1856]. The equation relates a volumetric flow rate to a fluid pressure gradient using a coefficient called the permeability. Permeability is a property of the medium and is therefore independent of the fluid used in its determination. Darcy's law is valid for all porous media as long as the volumetric flow rate is linearly proportional to the fluid pressure gradient, i.e. the flow is laminar. For instances of nonlaminar flow, auxiliary corrections are required to derive the "true" (Darcian) permeability of a medium from pressure and flow rate data. For example, when measuring materials with very high permeabilities and/or using pore fluids with very low viscosities, fluid flow can be turbulent. In this regime, a new parameter is introduced in order to account for inertial forces: this is known as the Forchheimer correction [Forchheimer, 1901]. Another instance where the relationship between volumetric flow rate and fluid pressure gradient is nonlinear is specific to measurements using gas. When the mean free path of the molecules/atoms approaches the characteristic pore or aperture size, interactions between the gas molecules/atoms and the pore walls serve to reduce resistance to flow, a phenomenon known as "slip flow" or "gas slippage". In this case, the apparent permeability is corrected using the Klinkenberg correction [Klinkenberg, 1941].

Most of the experimental studies designed to measure the permeability of volcanic rocks use an inert gas as the pore fluid; only a handful of studies have used water [e.g., Kolzenburg et al., 2012; Kendrick et al., 2013; Heap et al., 2014a, 2014b; Gaunt et al., 2014]. To the knowledge of the authors, there are no studies that compare gas and water permeabilities in volcanic materials. Laboratory measurements have shown that permeabilities to liquid water and gas are essentially equal for granite

* Corresponding author.
E-mail address: heap@unistra.fr (M.J. Heap).

https://doi.org/10.1016/j.jvolgeores.2018.02.002
0377-0273/

[Brace et al., 1968; Zhang et al., 2000]. A difference between permeabilities to gas and water has been observed for rocks containing mineral constituents that can react with the pore fluid, such as the reaction between liquid water and clay [Faulkner and Rutter, 2000, 2003; Tanikawa and Shimamoto, 2006; Davy et al., 2007; Tanikawa and Shimamoto, 2009; Behnsen and Faulkner, 2011] or the reaction between CO_2-enriched water and calcite [Noiriel et al., 2004; Luquot and Gouze, 2009]. These studies have shown, for example, that permeabilities to gas and liquid water in clay-rich rocks can differ by as much as an order of magnitude [e.g., Faulkner and Rutter, 2000]. A higher permeability to gas in clay-rich rocks is explained by the expansion of clay minerals in the presence of water due to water adsorption – the swollen clay minerals effectively constrict pore throats thus reducing permeability [Faulkner and Rutter, 2003].

It is often assumed, after the appropriate corrections have been applied, that permeabilities to gas and water are equivalent for materials for which significant physicochemical reactions are not expected. However, a lack of data comparing the gas and water permeabilities of a range of materials obscures a complete understanding. For example, the complex microstructure presented by volcanic rocks—often a complex network of pores and microcracks [Heap et al., 2014a; Farquharson et al., 2015; Colombier et al., 2017]—may yield a difference in permeabilities to gas and water in the absence of significant physicochemical reactions. The phase (gas or liquid) of the fluids within a porous volcanic system varies in time and space [e.g., Giggenbach and Soto, 1992; Taran et al., 1998; Chiodini et al., 2000; Byrdina et al., 2014], exemplified by the occurrence of phreatic and phreatomagmatic eruptions that are driven by the boiling of liquid water [e.g., Houghton and Nairn, 1991; Barberi et al., 1992; Mayer et al., 2015; Montanaro et al., 2016]. As a result, quantifying potential differences in the permeability to gas and water in volcanic rocks emerges as an important, yet unexplored, avenue for research. With this in mind, we present herein a study in which we measured the gas and water permeabilities of samples of andesite and basalt.

2. Description of experimental materials

For the purpose of this study, we selected a suite of variably porous andesites from Volcán de Colima (Mexico) and a well-studied basalt from Mt. Etna (Italy). Volcán de Colima is an active andesitic stratovolcano located at the western end of the Trans-Mexican Volcanic Belt in Mexico [Varley and Komorowski, 2018] and Mt. Etna is an active basaltic stratovolcano located on the east coast of the island of Sicily (Italy) [Allard et al., 2006].

The five andesite blocks used in this study (A5, B4, B5, C8, and LAH4) have been used in a number of recent studies focussed on the mechanical behaviour of andesite [e.g., Kendrick et al., 2013; Heap et al., 2014a, 2015]. Using the classification scheme of Farquharson et al. [2015], sample B5 can be classified as an "altered lava" (B5 displays high-temperature alteration, as evidenced by the presence of cristobalite; Fig. 1a), while the remaining blocks can be classified as "lava". The andesites all have a porphyritic texture consisting of a glassy groundmass (with abundant microlites) that hosts pores and a phenocryst cargo (Fig. 1). The porosity within these andesites comprises a combination of microcracks and pores (Fig. 1) [Kendrick et al., 2013; Heap et al., 2014a, 2015]. As evident in the scanning electron microscope (SEM) images of Fig. 1, the andesites contain a microcrack network that is both pervasive and tortuous. Indeed, microcrack densities range between 35 and 45 mm^{-1} [Heap et al., 2014a]. The microcracks are typically thin (no more than a few microns) and are usually no longer than 0.5 mm in length (Fig. 1). The andesites also contain high pore number densities, between 3.3 and 8.1 mm^{-2} [Heap et al., 2014a]. The pores are often far from spherical (Fig. 1) and are, in the case of the lowest porosity sample (B5), coated with cristobalite crystals (Fig. 1a). All of the andesites show a wide range of pore diameters, from 1 to 2 mm to a few tens of microns [Heap et al., 2014a].

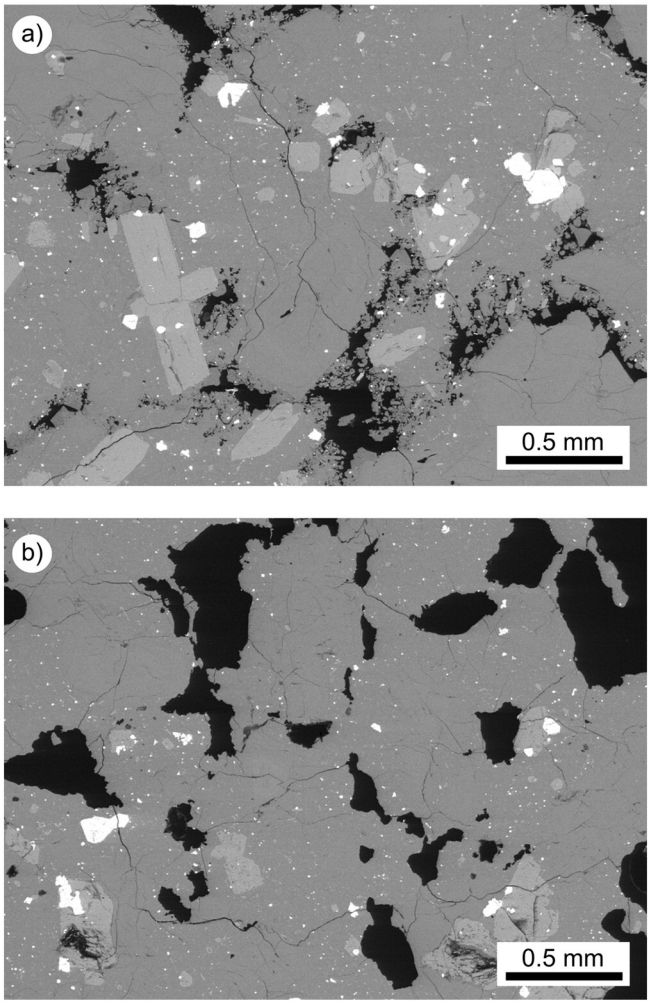

Fig. 1. (a) Backscattered scanning electron microscope image of andesite sample B5 (from Volcán de Colima, Mexico). (b) Backscattered scanning electron microscope image of andesite sample C8 (from Volcán de Colima). Both samples are characterised by a complex microstructure containing both pores and microcracks (see text for details).

The basalt from Mt. Etna has porphyritic texture consisting of a completely crystallised groundmass containing pores and a phenocryst cargo (Fig. 2). This basalt has been the focus of a number of studies in the last ten years [e.g., Vinciguerra et al., 2005; Stanchits et al., 2006; Heap et al., 2011; Zhu et al., 2016]. The porosity within the basalt comprises a combination of microcracks and pores (Fig. 2). Qualitatively, the microcracks in the basalt are typically much longer (often several mm) than those in the andesites (Figs. 1 and 2). The microcracks within the basalt often traverse through both the crystallised groundmass and the large phenocrysts present within the sample (Fig. 2a). The pores within the basalt are not distributed throughout the sample, but are present in pockets (Fig. 2b). The pores within these porous pockets represent the volume between microlites where the groundmass is absent, a texture termed diktytaxitic [see, for example, Kushnir et al., 2016]. The pores are typically <100 μm in diameter (Fig. 2b).

3. Experimental methods

Cylindrical samples (20 mm in diameter and precision-ground to a nominal length of 40 mm) were prepared from the five blocks of andesite (A5, B4, B5, C8, and LAH4) and the block of basalt. These samples were then dried in a vacuum oven at 40 °C for at least 48 h. Before measuring their permeability, the prepared 20 mm-diameter samples were first investigated in terms of their connected porosity (using helium

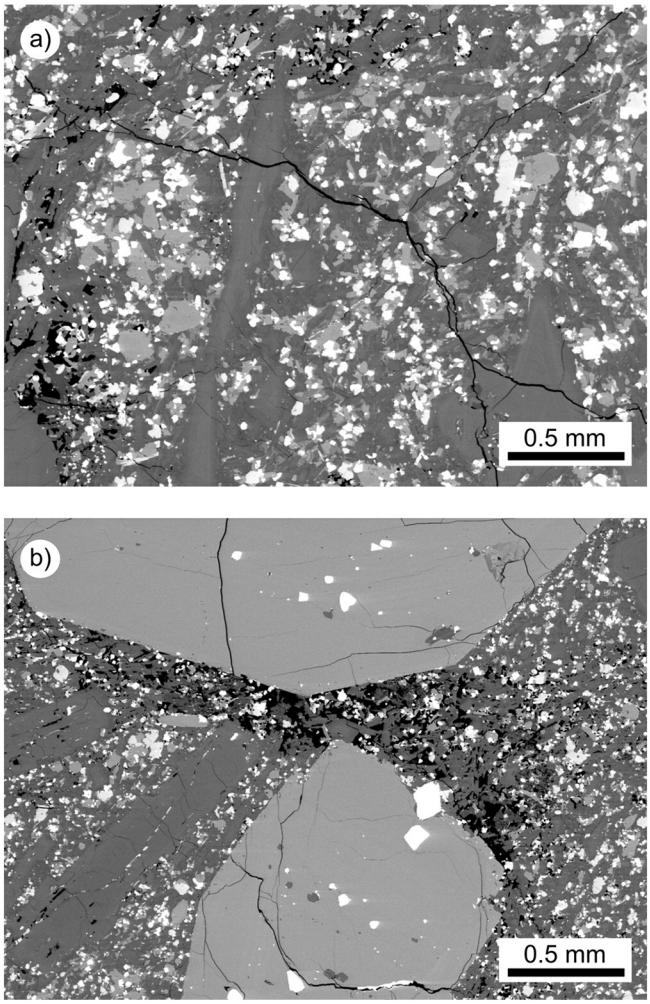

Fig. 2. (a) Backscattered scanning electron microscope image of the basalt from Mt. Etna (Italy) showing a long microcrack that traverses the crystallised groundmass. (b) Backscattered scanning electron microscope image of the basalt from Mt. Etna showing a pocket of micropores sandwiched between two phenocrysts (see text for details).

pycnometry) and specific surface area (using Brunauer, Emmett, and Teller (BET) gas adsorption measurements).

The connected porosity of each sample was measured using the skeletal (connected) volume provided by a helium pycnometer (Micromeritics AccuPyc II 1340) (values are an average of 20 measurements; precision ±0.00005 cm^3) and the bulk volume determined using the sample dimensions (precision ±0.005 mm). The specific surface area was determined using BET nitrogen or krypton adsorption measurements [Brunauer et al., 1938]. The samples were placed a vacuum sealed vessel (itself placed in a liquid nitrogen bath at a temperature of −196.15 °C) and the specific surface area was calculated by determining the amount of adsorbate gas needed to create a monomolecular layer on the connected surface inside the sample. The absorbent gas used for the basalt was nitrogen. Krypton gas was used for the andesite samples due to their low specific surface areas (krypton is better suited for samples with low specific surface areas due to its smaller molecular size). More details on the BET method and theory employed here can be found in Brunauer et al. [1938] and Kushnir et al. [2016].

To assess their pore throat structure, mercury injection porosimetry was performed on pieces (~5 g) of two of the andesite blocks (B5 and C8) and the basalt using the Micromeritics Autopore IV 9500 at the University of Aberdeen (Scotland). The evacuation pressure and evacuation time were 50 μmHg and 5 min, respectively, and the mercury filling pressure and equilibration time were 0.52 pounds per square inch absolute (psia) and 10 s, respectively. The pressure range was 0.1 to 60,000 psia (i.e. up to a pressure of about 400 MPa). Mercury injection data permit the calculation of the pore throat size distribution within a particular sample. The mercury injection data were corrected for the "low pressure correction" recommended by ASTM International [ASTM D4404-10, 2010].

The permeabilities to gas (argon) and water (deionised water) were then measured on the prepared cylindrical samples. We first performed a suite of gas and water permeability measurements on the variably porous andesite samples at a confining pressure of 2 MPa. We then performed gas and water permeability measurements at a range of confining pressures (from 1 to 50 MPa) on a sample of andesite (B5) and a basalt sample. To avoid problems associated with potential permanent microstructural changes following exposure to 50 MPa, we used different samples (cored from the same block) for the gas and water permeability measurements in these latter experiments. The pairs of samples for these experiments were selected based on their almost identical initial permeabilities (measured with inert gas at a confining pressure of 1 MPa).

Samples to be measured with water were first vacuum-saturated with deionised water. The saturation procedure consisted of three steps:

(1) The samples were vacuum-dried at 40 °C for at least 48 h,
(2) The samples were then immediately placed inside a belljar which was then vacuumed for at least 12 h and, finally,
(3) Degassed (using a Venturi siphon with municipal water as the motive fluid), deionised water was introduced into the belljar (while under vacuum).

Great care was taken to ensure that the water was fully degassed and that the samples were fully saturated. Once prepared, the samples were jacketed in a viton sleeve and placed inside a hydrostatic pressure vessel. The confining pressure (P_c) was then increased to 2 MPa (for the set of measurements on the variably porous andesite sample suite) or 1 MPa (for the measurements to be performed at different confining pressures). The samples were left overnight at this pressure to allow for microstructural equilibration. All measurements of water permeability were performed using the steady-state flow method. Following microstructural equilibrium, a pressure gradient was imposed across the sample and the flow rate measured using an electronic balance (with a precision ±0.0005 g). Once steady-state flow had been established, the water permeability k_{water} was determined using Darcy's relation:

$$\frac{Q}{A} = \frac{k_{water}}{\eta L}(P_{up} - P_{down}), \quad (1)$$

where Q is the volumetric flow rate, A is the cross-sectional area of the sample, P_{up} and P_{down} represent the upstream and downstream pressure, respectively (where P_{down} is the atmospheric pressure), L is the length of the sample, k_{water} is the permeability to water, and η is the viscosity of the pore fluid (taken here as 1.008×10^{-3} Pa·s). A pressure gradient (i.e. $P_{up} - P_{down}$) of 0.5 MPa was used for all of the steady-state measurements using water as the pore fluid (i.e. the mean pore fluid pressure, P_m, was 0.35 MPa, where $P_m = (P_{up} + P_{down})/2$).

Gas (argon) permeability was measured using either the steady-state method (for the andesites) or the pulse-decay method (for the basalt). The method chosen was based on the permeability of the sample: the steady-state method is better suited for high-permeability samples and the pulse-decay method is better suited for low-permeability samples (we note that there is no experimental bias between the methods: the permeability values of samples of intermediate permeability measured using both techniques in our laboratory are essentially identical). For the steady-state method, a pressure gradient was imposed across the sample (following microstructural equilibrium) and the outlet flow rate was measured using one of three Bronkhorst flowmeters.

The choice of flowmeter depended on the permeability of the sample and therefore volumetric flow rate (the volumetric flow rate range for the three flowmeters: 1, 3, and 125 ml/min). Since the pore fluid is compressible, the raw permeability to gas k_{gas_raw} is expressed as [Scheidegger, 1974]:

$$\frac{Q}{A} = \frac{k_{gas\_raw}}{\eta L} \frac{(P_{up})^2 - (P_{down})^2}{2P_{down}}, \quad (2)$$

where η, the viscosity of the pore fluid, was taken as 2.21×10^{-5} Pa·s. Steady-state volumetric flow rate Q measurements were taken under several pore pressure gradients (i.e. $P_{up} - P_{down}$, where P_{down} is the atmospheric pressure) to check whether any auxiliary corrections were required. The magnitude of pore pressure gradients used for the gas steady-state measurements varied depending on the permeability of the sample, but never exceeded 0.5 MPa (i.e. $P_m \leq 0.35$ MPa). We first plot $1/k_{gas\_raw}$ as a function of Q to check whether the Forchheimer correction is required. The correction is necessary if these data can be well described by a positive linear slope. The Forchheimer-corrected permeability is taken as the inverse of the y-intercept of the best-fit linear regression in the plot of $1/k_{gas\_raw}$ as a function of Q. An example of data that required the Forchheimer correction is shown in Fig. 3a (for sample LAH4_7). If the Forchheimer correction is not required, we then check whether the Klinkenberg correction is required. To do so, we plot k_{gas_raw} as a function of the reciprocal mean pressure, $1/P_m$. The Klinkenberg correction is required if these data can be well described by a positive linear slope and, if true, the Klinkenberg-corrected permeability can be taken as the y-intercept of the best-fit linear regression in the plot of k_{gas_raw} as a function of $1/P_m$. The Forchheimer correction was required for the high-porosity andesites (Table 1) and the Klinkenberg correction was required for the low-porosity andesites (Table 1).

We used the pulse decay method [Brace et al., 1968] to measure the gas permeability of the basalt sample. Following microstructural equilibrium at the target confining pressure, the decay of an initial pore pressure differential ($P_{up} - P_{down} = 0.5$ MPa, where P_{down} is the atmospheric pressure; i.e. $P_m = 0.35$ MPa at the start of the experiment and decayed to the atmospheric pressure with time) was monitored using a pressure transducer following the closure of the upstream pressure inlet. The gas permeability k_{gas_raw} was then determined using the following relation:

$$k_{gas\_raw} = 2\frac{\eta L}{A} \frac{V_{up}}{{P_{up}}^2 - {P_{down}}^2} \frac{dP_{up}}{dt}, \quad (3)$$

where V_{up} is the volume of the upstream pore pressure circuit ($=7.8 \times 10^{-6}$ m^3) and t is time. As before, we checked whether these data required any auxiliary corrections (the Forchheimer or Klinkenberg correction). We found that the Klinkenberg correction was required for all of the basalt measurements (Table 1). An example of data that required the Klinkenberg correction is shown in Fig. 3b (for sample EB_3).

Each permeability measurement was remeasured the following day. The sample was only removed, or subjected to the next confining pressure increment, if the retrieved permeability was the same as for the previous day. All the measurements in this study were performed under ambient laboratory temperatures.

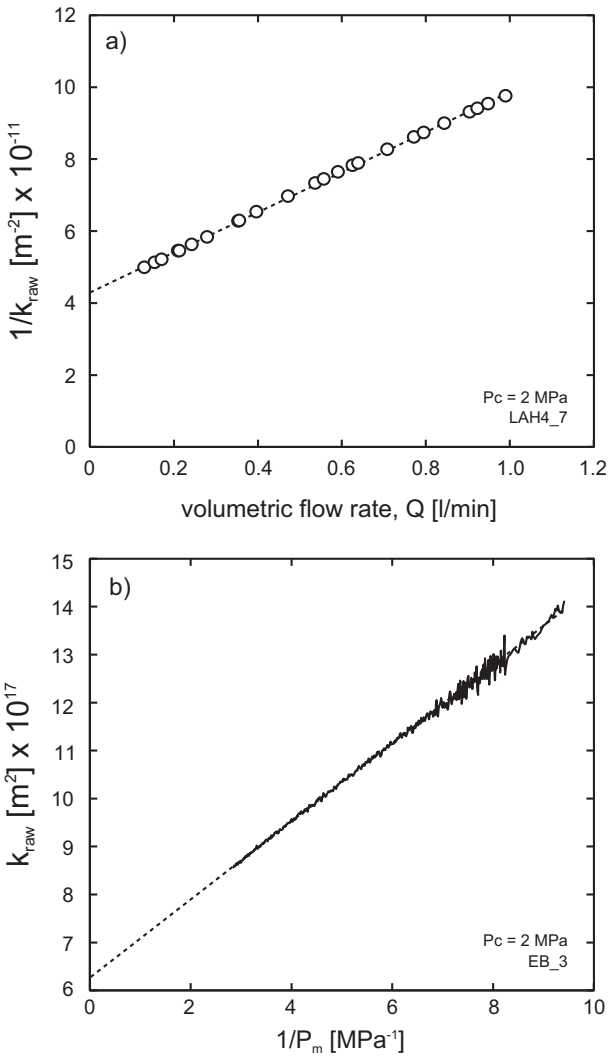

Fig. 3. (a) Data that require a Forchheimer correction. The graph is a plot of $1/k_{gas\_raw}$ as a function of volumetric flow rate, Q. The Forchheimer correction is necessary if the data can be well described by a positive linear slope. The Forchheimer-corrected permeability is taken as the inverse of the y-intercept of the best-fit linear regression. In the example shown here, the permeability is 2.33×10^{-12} m^2 (Table 1). (b) Data that require a Klinkenberg correction. The graph is a plot of k_{gas_raw} as a function of the reciprocal mean pressure $1/P_m$, where P_m is the mean pore fluid pressure (i.e. $(P_{up} + P_{down})/2$). The Klinkenberg correction is required if the data can be well described by a positive linear slope and, if true, the Klinkenberg-corrected permeability is taken as the y-intercept of the best-fit linear regression. In the example shown here, the permeability is 6.29×10^{-17} m^2 (Table 1).

4. Results

4.1. Connected porosity, specific surface area, and pore throat size distribution

The connected porosities of the andesite samples ranged from 0.08 to 0.27 and the connected porosities of the basalt samples were measured to be 0.04 (Table 1).

The specific surface area of the andesites varied from 15 to 100 m^2 kg^{-1} (Table 1). We note that the specific surface area does not correlate with connected porosity: the andesite with the highest specific surface area (B5; Fig. 1a) contains one of the lowest porosities (Table 1). The specific surface of the basalt block was measured to be 126 m^2 kg^{-1} (Table 1).

Mercury porosimetry, which provides the pore throat size distribution, was performed on a low-porosity (B5) and a high-porosity (C8) andesite (Fig. 4a) and the basalt (Fig. 4b). About 50% of the porosity in andesite sample C8 (porosity = 0.144) is connected by pore throats with a radius ≥ 5 μm. Pore throats with a radius ≥ 5 μm connect only 35% of the porosity in andesite sample B5 (porosity = 0.076) (Fig. 4a). Only 10% of the porosity in samples C8 and B5 is connected by pore throats with radii ≤0.5 μm (Fig. 4a). The average pore throat radius was determined to be 2.15 and 1.05 μm for andesites C8 and B5, respectively. The mercury porosimetry data for the basalt show that 65% of the porosity is connected by pore throats with a radius below 0.5 μm

Table 1
Summary of the experimental data collected for this study. Steady-state permeabilities were collected under a pressure gradient of 0.5 MPa. The pressure gradient at the start of the pulse decay measurements was 0.5 MPa. *Specific surface area of this sample was not measured and is assumed here to be equal to that of sample B5_5. **Specific surface areas of these samples were not measured and are assumed here to be equal to that of another measured sample (EB_7).

Sample	Connected porosity	Specific surface area ($m^2\ kg^{-1}$)	Method	Confining pressure (MPa)	Permeability to water (m^2)	Permeability to gas (m^2)	Permeability to gas/permeability to water	Klinkenberg slip factor, b (MPa)	Average pore diameter determined using b (μm)
B4_2	0.082	26	Steady-state	2	1.09×10^{-15}	1.17×10^{-15}	1.07	0.503	0.054
B5_5	0.085	100	Steady-state	2	3.13×10^{-15}	3.97×10^{-15}	1.27	0.069	0.396
A5_11	0.089	15	Steady-state	2	1.49×10^{-15}	1.69×10^{-15}	1.13	0.204	0.134
A5_1	0.100	16	Steady-state	2	6.55×10^{-15}	7.61×10^{-15}	1.16	0.134	0.204
A5_7	0.137	20	Steady-state	2	1.48×10^{-13}	5.14×10^{-13}	3.47	Forchheimer	–
C8_9	0.166	35	Steady-state	2	1.04×10^{-13}	5.68×10^{-13}	5.46	Forchheimer	–
C8_8	0.193	28	Steady-state	2	6.51×10^{-13}	1.52×10^{-12}	2.33	Forchheimer	–
LAH4_7	0.253	51	Steady-state	2	1.34×10^{-12}	2.33×10^{-12}	1.74	Forchheimer	–
LAH4_9	0.267	57	Steady-state	2	1.05×10^{-12}	1.76×10^{-12}	1.68	Forchheimer	–
B5_5	0.081	100	Steady-state	1	–	5.36×10^{-15}	–	0.054	0.507
B5_5	0.081	100	Steady-state	2	–	4.66×10^{-15}	–	0.060	0.456
B5_5	0.081	100	Steady-state	5	–	3.65×10^{-15}	–	0.082	0.334
B5_5	0.081	100	Steady-state	10	–	2.82×10^{-15}	–	0.100	0.274
B5_5	0.081	100	Steady-state	15	–	2.45×10^{-15}	–	0.111	0.246
B5_5	0.081	100	Steady-state	20	–	2.23×10^{-15}	–	0.115	0.238
B5_5	0.081	100	Steady-state	25	–	2.06×10^{-15}	–	0.120	0.228
B5_5	0.081	100	Steady-state	30	–	1.97×10^{-15}	–	0.120	0.228
B5_5	0.081	100	Steady-state	35	–	1.79×10^{-15}	–	0.123	0.222
B5_5	0.081	100	Steady-state	40	–	1.77×10^{-15}	–	0.119	0.230
B5_5	0.081	100	Steady-state	45	–	1.73×10^{-15}	–	0.116	0.236
B5_5	0.081	100	Steady-state	50	–	1.73×10^{-15}	–	0.112	0.244
B5_21	0.085	100*	Steady-state	1	1.51×10^{-15}	–	–	–	–
B5_21	0.085	100*	Steady-state	2	1.33×10^{-15}	–	–	–	–
B5_21	0.085	100*	Steady-state	5	1.09×10^{-15}	–	–	–	–
B5_21	0.085	100*	Steady-state	10	9.47×10^{-16}	–	–	–	–
B5_21	0.085	100*	Steady-state	15	8.55×10^{-16}	–	–	–	–
B5_21	0.085	100*	Steady-state	20	7.82×10^{-16}	–	–	–	–
B5_21	0.085	100*	Steady-state	25	7.07×10^{-16}	–	–	–	–
B5_21	0.085	100*	Steady-state	30	6.82×10^{-16}	–	–	–	–
B5_21	0.085	100*	Steady-state	35	6.53×10^{-16}	–	–	–	–
B5_21	0.085	100*	Steady-state	40	6.30×10^{-16}	–	–	–	–
B5_21	0.085	100*	Steady-state	45	6.02×10^{-16}	–	–	–	–
B5_21	0.085	100*	Steady-state	50	5.52×10^{-16}	–	–	–	–
EB_3	0.041	126**	Pulse-decay	1	–	8.40×10^{-17}	–	0.096	0.285
EB_3	0.041	126**	Pulse-decay	2	–	6.29×10^{-17}	–	0.129	0.212
EB_3	0.041	126**	Pulse-decay	5	–	4.83×10^{-17}	–	0.143	0.191
EB_3	0.041	126**	Pulse-decay	10	–	3.49×10^{-17}	–	0.162	0.169
EB_3	0.041	126**	Pulse-decay	15	–	2.69×10^{-17}	–	0.174	0.157
EB_3	0.041	126**	Pulse-decay	20	–	2.14×10^{-17}	–	0.184	0.149
EB_3	0.041	126**	Pulse-decay	25	–	1.81×10^{-17}	–	0.187	0.146
EB_3	0.041	126**	Pulse-decay	30	–	1.51×10^{-17}	–	0.199	0.137
EB_3	0.041	126**	Pulse-decay	35	–	1.31×10^{-17}	–	0.201	0.136
EB_3	0.041	126**	Pulse-decay	40	–	1.15×10^{-17}	–	0.206	0.133
EB_3	0.041	126**	Pulse-decay	45	–	9.89×10^{-18}	–	0.208	0.131
EB_3	0.041	126**	Pulse-decay	50	–	8.73×10^{-18}	–	0.214	0.128
EB_5	0.041	126**	Steady-state	1	1.87×10^{-17}	–	–	–	–
EB_5	0.041	126**	Steady-state	2	1.53×10^{-17}	–	–	–	–
EB_5	0.041	126**	Steady-state	5	1.23×10^{-17}	–	–	–	–
EB_5	0.041	126**	Steady-state	10	8.82×10^{-18}	–	–	–	–
EB_5	0.041	126**	Steady-state	15	6.70×10^{-18}	–	–	–	–
EB_5	0.041	126**	Steady-state	20	5.55×10^{-18}	–	–	–	–
EB_5	0.041	126**	Steady-state	25	4.51×10^{-18}	–	–	–	–
EB_5	0.041	126**	Steady-state	30	3.70×10^{-18}	–	–	–	–
EB_5	0.041	126**	Steady-state	35	3.44×10^{-18}	–	–	–	–
EB_5	0.041	126**	Steady-state	40	2.94×10^{-18}	–	–	–	–
EB_5	0.041	126**	Steady-state	45	2.46×10^{-18}	–	–	–	–
EB_5	0.041	126**	Steady-state	50	2.20×10^{-18}	–	–	–	–

(Fig. 4b). The average pore throat radius for the basalt was determined to be 0.17 μm.

4.2. Influence of porosity on gas and water permeabilities

Gas and water permeabilities were measured for a suite of variably porous andesites from Volcán de Colima (Fig. 5; Table 1). These measurements were all collected under a constant confining pressure of 2 MPa. First, and as observed in previous studies [e.g., Farquharson et al., 2015], permeability is higher at higher porosities. Our data further show that gas permeability is higher than water permeability over the entire porosity range (0.08 to 0.27) (Fig. 5; Table 1). The difference between gas and water permeability is between a factor of 1.1 and 5.5 (Fig. 5; Table 1).

4.3. Influence of confining pressure on gas and water permeabilities

Gas and water permeabilities were measured on a sample of andesite (B5) and a sample of basalt as a function of confining pressure (from 1 to 50 MPa) (Fig. 6; Table 1). For both samples, and both pore fluids,

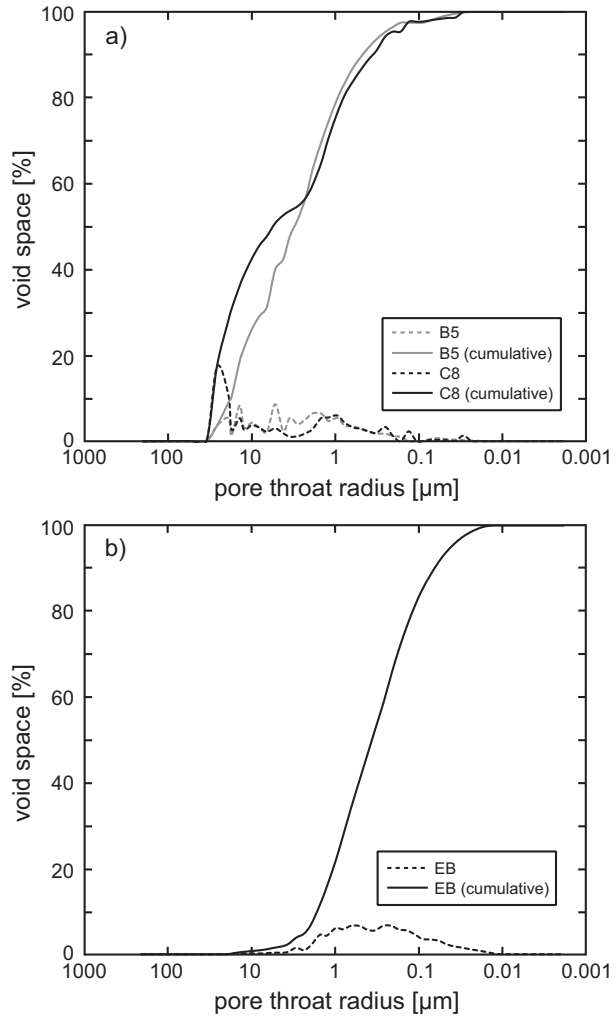

Fig. 4. (a) Pore throat radius distributions, determined by mercury injection, for andesite samples B5 and C8 (from Volcán de Colima, Mexico). (b) Pore throat radius distribution, determined by mercury injection, for the basalt from Mt. Etna (Italy). Dashed curves show the void space and the solid curves show the cumulative void space. The mercury injection data was corrected for the 'low pressure correction' recommended by ASTM International [ASTM D4404-10, 2010].

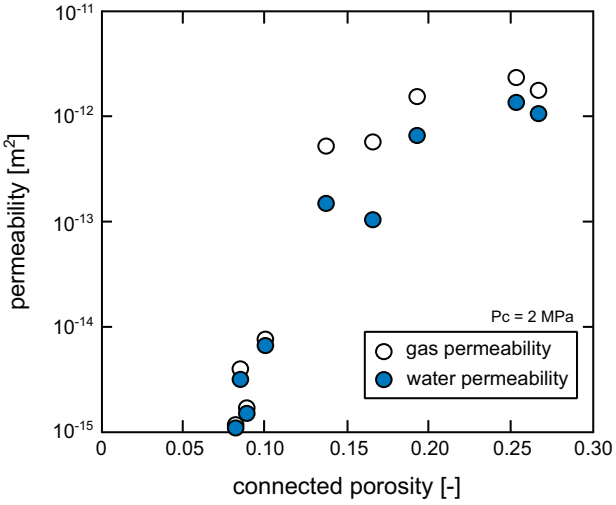

Fig. 5. Gas (white circles) and water (blue circles) permeability as a function of connected porosity for a suite of andesites from Volcán de Colima (Mexico). All measurements were performed under a confining pressure of 2 MPa. Error due to transducer precision is smaller than the symbol size. Data available in Table 1.

large decreases in permeability are observed between 1 and 10 MPa (Fig. 6). At confining pressures of 15 MPa and above, the permeability decrease per increment of confining pressure is reduced (Fig. 6). We also note that the absolute decrease in permeability from 1 to 50 MPa is much greater in the basalt than in the andesite: an order of magnitude in the case of the former and only a factor of three for the latter (Fig. 6; Table 1). The difference between gas and water permeabilities is about a factor of three for the andesite and about a factor of four for the basalt (Table 1). For both rock types, this offset does not change significantly as confining pressure is increased (Fig. 6; Table 1).

5. Discussion

A difference in permeability when using different fluids is usually considered the consequence of a physicochemical reaction between the mineral constituents of the rock and the pore fluid, such as the reaction between liquid water and clay [Faulkner and Rutter, 2000, 2003; Tanikawa and Shimamoto, 2006; Davy et al., 2007; Tanikawa and Shimamoto, 2009; Behnsen and Faulkner, 2011] or the reaction between CO_2-enriched water and calcite [Noiriel et al., 2004; Luquot and Gouze, 2009]. It is for this reason that gas and water permeabilities are rarely measured and compared when the rock-forming minerals are not expected to react with the pore fluid. One such study [Brace et al., 1968] showed that gas and water permeabilities are essentially equal in intact Westerly granite (porosity = 0.008) over a range of confining pressures between 10 and 100 MPa. Our new data show that gas and water permeabilities can differ in volcanic rocks by up to a factor of five (Figs. 5 and 6). Since these volcanic rocks do not contain minerals (such as clay) that are expected to undergo significant physicochemical reactions in the presence of water, there must be another explanation for the measured difference in gas and water permeability.

To better understand the microstructural path taken by the gas, we can use the Klinkenberg slip factor, b, (which has the units of pressure) [Klinkenberg, 1941] to provide an estimate of the average radius of the pores used by the gas molecules. The Klinkenberg slip factor has previously been used to examine the average pore radius of the flow path in low-porosity rocks such as shales [e.g., Heller et al., 2014; Firouzi et al., 2014; Letham and Bustin, 2016]. Since the mean free path is inversely proportional to P_m, Poiseuille's law for gas flow in a cylindrical tube and Darcy's law for flow in porous media yields the following relation:

$$k_{gas} = k_{gas\_raw}\left(1 + \frac{b}{P_m}\right), \tag{4}$$

where k_{gas} is the true (Klinkenberg-corrected) gas permeability. Therefore, and assuming tube-shaped pores, the average pore radius r can be estimated using the following relation [Civan, 2010]:

$$r = \frac{4}{b}\eta\sqrt{\frac{\pi R_g T}{2M_w}}, \tag{5}$$

where R_g is the ideal gas constant (taken as 8.31 J mol^{-1} K^{-1}), T is the temperature (taken as 293 K), and M_w is the molecular mass of the pore fluid (taken as 0.03995 kg mol^{-1}). The average pore radius that controls the flow of gas molecules (calculated using Eq. (5)) for the sample of andesite (B5) and basalt as a function of confining pressure is shown in Fig. 7. The calculations show that the average pore radius in the andesite is ~0.5 μm at low pressure (between 1 and 2 MPa) and evolves to, and stays constant at, ~0.2–0.25 μm when the confining pressure is at or above 15 MPa (Fig. 7; Table 1). The average pore radius in the basalt is ~0.3 μm at a confining pressure of 1 MPa (Fig. 7; Table 1). The average pore radius in the basalt reduces to, and stays constant at, ~0.13–0.16 μm when the confining pressure is at or above 15 MPa

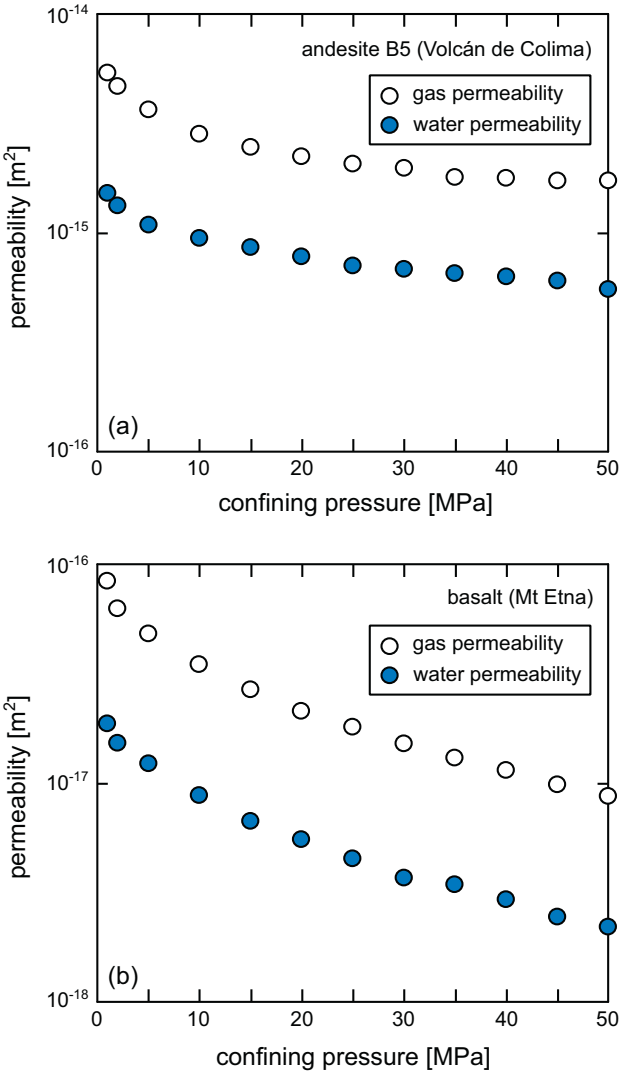

Fig. 6. Gas (white circles) and water (blue circles) permeability as a function of confining pressure (from 1 to 50 MPa) for (a) andesite sample B5 (from Volcán de Colima, Mexico) and (b) the basalt from Mt. Etna (Italy). Error due to transducer precision is smaller than the symbol size. Data available in Table 1.

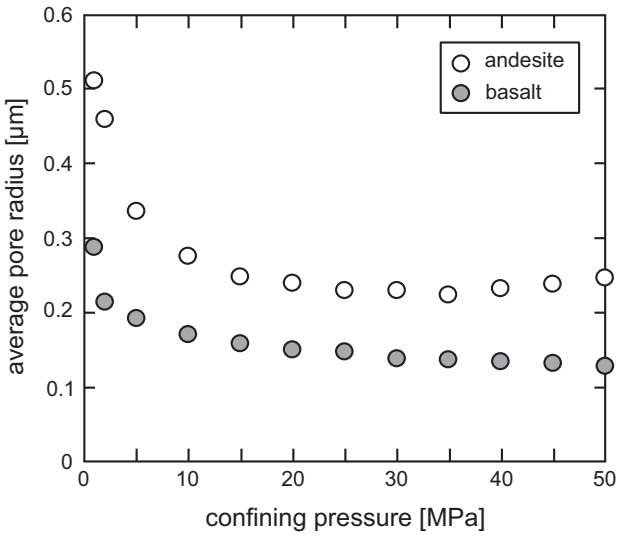

Fig. 7. Average pore radius for andesite sample B5 (from Volcán de Colima, Mexico) (white circles) and the basalt from Mt. Etna (Italy) (grey circles) as a function of confining pressure (from 1 to 50 MPa), as calculated using the Klinkenberg slip factor (see Eq. (5) and text for details). Data available in Table 1.

(Fig. 7; Table 1). The Klinkenberg slip factor can also be used to estimate the width of "slit-shaped" pores (i.e. microcracks) [e.g., Heller et al., 2014; Letham and Bustin, 2016], which, according to our microstructural analyses (Figs. 1 and 2) and mercury injection data (Fig. 4), may better suit these rocks, especially the basalt (Figs. 2 and 4b). However, the widths predicted using the equation presented in Heller et al. [2014] and Letham and Bustin [2016] are within the range ~3–11.5 and ~3–6.5 μm for the andesite and basalt, respectively. We consider such widths unrealistically high. The basalt, for example, not only has an average pore throat diameter of 0.34 μm (determined by mercury porosimetry), but the mercury injection data also show that only ~2% of the void space is connected by pore throats with diameters larger than 6.5 μm (Fig. 4b). Although it is difficult at present to forward a reason as to why the average width of a slit-shaped pore provides an overestimation of the size of the microstructural elements carrying the gas, while the average radius of a tube-shaped pore does not, we highlight that these geometries only represent end-member geometries in rocks characterised by geometrically complex pore networks (Figs. 1, 2, and 4). As a result, although the average pore radii provided in Fig. 7 inform on the size of the microstructural element used by the gas molecules (i.e. submicron), we highlight that these values are estimations that assume a cylindrical pore shape. The average pore radius used by the gas molecules in the basalt predicted using Eq. 5 (~0.13–0.3 μm; Fig. 7) is very similar to the average pore throat radius determined by the mercury porosimetry (0.17 μm). This is likely a consequence of the relatively narrow range of pore and pore throat sizes (Fig. 4b) within the basalt: 80% of the void space is connected by pore throat radii between ~0.7 and ~1.5 μm (Fig. 4b). However, the average pore throat radius determined by mercury porosimetry is 2.15 and 1.05 μm for andesites C8 and B5, respectively, much greater than the radii predicted using the Klinkenberg slip factor (~0.25–0.5 μm; Fig. 7). Although the andesites contain microstructural elements (microcracks and tubes) of varying diameter (Fig. 4a), resulting in a high average pore throat radius, pores within this size range are likely not used for flow, which is likely obliged to negotiate through narrow microstructural elements (on the submicron scale).

Based on the mercury porosimetry (Fig. 4) and the average pore radii (assuming a cylindrical pore shape) predicted using Eq. (5) (Fig. 7), it is likely that the gas in both samples (andesite and basalt) is travelling through thin and tortuous/rough microcracks. This inference is supported by the evolution of permeability as confining pressure increases (Fig. 6). A reduction in the permeability of microcracked volcanic rocks with increasing confining pressure has been previously explained by the narrowing of microcrack apertures or the closing of microcracks [e.g., Vinciguerra et al., 2005; Nara et al., 2011; Fortin et al., 2011; Heap et al., 2017], supported here by the decrease in our average pore radii estimations with increasing confining pressure (Fig. 7). However, the reductions in permeability with confining pressure for the volcanic rocks studied herein (Fig. 6) are much less than those typically observed for microcracked granites [e.g., Le Ravalec et al., 1996; David et al., 1999; Darot and Reuschlé, 2000]. We consider this a consequence of the tortuous/rough nature of the microcracks within the studied andesite and basalt (Figs. 1 and 2): tortuous and rough cracks require higher pressures to close than straight and smooth cracks [e.g., Pérez-Flores et al., 2017]. Further, the more significant decrease in the permeability of the basalt with increasing confining pressure—one order of magnitude compared to a factor of three in the andesite (Fig. 6)—must require that the microcracks supporting fluid flow in the andesite are more difficult to close than those in the basalt. Indeed, qualitative microstructural observations suggest that the microcracks in the andesite are shorter and more tortuous/kinked than those in the basalt (Figs. 1 and 2), adding confidence to this hypothesis.

The estimations of average pore radii shown in Fig. 7, and the average pore throat radii determined from the mercury porosimetry data, highlight the microstructural complexity of volcanic rocks. To emphasise, although ~90% of the void volume in the andesite is connected by pore throats >1 μm (Fig. 4a), our pore radii predictions (Fig. 7) suggest the gas flow is controlled by microstructural elements that have an average radius of ~0.2–0.25 μm. To the authors' knowledge, this represents the first time the Klinkenberg slip factor has been used to estimate the average pore radius of gas flow paths in volcanic materials; we recommend that this method is utilised in future studies.

We must now consider why these thin microstructural elements could be inaccessible to water. Faulkner and Rutter [2000] inferred that the lower permeability to water than to gas in clay-bearing fault gouge was a result of layers of structured water adsorbed onto the phyllosilicate mineral surfaces, thereby reducing the effective pore throat aperture and reducing permeability. However, there are no clay minerals in our studied materials. The permeability experiments of Klinkenberg [1941], although designed to test the hypothesis that adsorbed molecules on the walls of small capillaries in porous materials could inhibit fluid flow, found that the permeabilities to different liquids were within experimental error. However, as discussed in Faulkner and Rutter [2000], any water adsorption effect in the high-permeability ($\sim 10^{-14}$ m^2) glass filters of Klinkenberg [1941] was likely masked by their large pore throat apertures. In other words, perhaps the pore radii of the volcanic rocks tested herein are sufficiently narrow to observe a difference due to water adsorption, while the apertures of glass filters tested by Klinkenberg [1941] are not. Although we cannot advance a definitive reason for the difference between gas and water permeability in the volcanic rocks measured herein, we speculate that water molecules adsorbed onto the surface of the thin (~0.1–0.5 μm) microstructural elements are capable of narrowing their aperture or rendering them inaccessible to the flow of water. It is the complex nature and poor connectivity of the void space in these volcanic rocks (Figs. 1, 2, and 4) that obliges fluid to negotiate these thin microstructural elements, which are also characterised by complex geometries (i.e. tortuous, kinked, and rough; see discussion above). We further speculate that it is the tortuous, kinked, and rough nature of the microcracks that allows the adsorption of water to reduce the water permeability. Adsorbed water molecules need not obstruct the entire length of a microcrack, but only a small section – perhaps a particularly rough-walled section or at a tight bend or kink. Although this complex microstructure is typical of lavas [e.g., Colombier et al., 2017], it is unclear at present whether volcanic rocks that contain a permeable backbone of large, well-connected tubes—such as some pumices—will also display differences between gas and water permeabilities.

The implication of these data is that the permeability of the rocks comprising a volcanic edifice will be higher to gas (e.g., CO_2 and SO_2; Edmonds et al., 2003) than to liquid (e.g., the infiltration of meteoric and seawater and the circulation of groundwater/hydrothermal fluids; Hurwitz et al., 2003). Further, permeability may vary in zones that experience fluctuations in pore fluid state as a result of fluctuating temperature or pressure. For example, a reduction in temperature that results in a change in fluid state from gas to liquid may promote pore pressure build-up as a result of a decrease in permeability. Alternatively, unloading of the edifice (due to mass movement events, for example) could trigger decompression of the interstitial pore fluid, prompting a phase change in the opposite direction (i.e. liquid to vapour). Importantly, the saturation curve for water (which delineates the pressure-temperature boundary between liquid and vapour) occurs within conditions relevant for a shallow edifice. Indeed, electrical resistivity tomography of the shallow hydrothermal system of Campi Flegrei (Italy) shows a complex configuration of gaseous and liquid zones, and zones characterised by mixtures of gases and liquids [Byrdina et al., 2014]. The data presented herein therefore have important ramifications for the distribution and build-up of pore pressure in a volcanic system. Further, the choice of pore fluid used in laboratory investigations and the choice of permeability values to be used in fluid flow modelling should be carefully considered [e.g., Collombet, 2009; Collinson and Neuberg, 2012; Fournier and Chardot, 2012; Chevalier et al., 2017]. Finally, we also highlight that care should be taken when collating porosity-permeability data from published studies.

6. Conclusions

Our laboratory measurements highlight that gas permeability can be a factor of two to five higher than water permeability in volcanic rocks. Using the Klinkenberg slip factor (assuming tube-shaped pores), we estimate the average radius of the microstructural elements used by the gas flow to be ~0.1–0.5 μm. Although we cannot definitively advance a reason for the difference in gas and water permeability, we speculate that water adsorption on the surfaces of these thin microstructural elements—assumed here to be microcracks—may reduce their effective radius and/or prevent access, thus reducing the water permeability of these volcanic rocks. We further speculate that it is the tortuous, kinked, and rough nature of the microcracks that allows the adsorption of water to reduce the water permeability. Adsorbed water molecules need not obstruct the entire length of a microcrack, but only a small section – perhaps a particularly rough-walled section or at a tight bend or kink. Our data highlight the need for further studies that explore differences between gas and water permeabilities in a range of volcanic materials. A difference between gas and water permeabilities in volcanic materials has important ramifications for the distribution and build-up of pore pressure in hydrothermal and geothermal systems in volcanically active regions, as well as volcanic systems themselves.

Acknowledgements

M.J. Heap acknowledges an Initiative d'Excellence (IDEX) “Attractivité” grant (VOLPERM) and P. Baud and J.I. Farquharson acknowledge an IDEX “Contrats doctoraux” grant, both funded by the University of Strasbourg. Gilles Morvan is thanked for his assistance using the SEM. We would like to thank S. Mueller, O. Spieler, and N. Varley for their role in collecting the andesites from Volcán de Colima in 2004 (field campaign supported by the R&D Programme GEOTECHNOLOGIEN, funded by the German Ministry of Education and Research (BMBF), and German Research Foundation (DFG) grant PTJ MGS/03G584A-SUNDAARC-DEVACOM). We thank P.G. Meredith for providing the samples of basalt from Mt. Etna. The mercury porosimetry was performed at the University of Aberdeen; thanks go to Dave Healy for providing the final measurement free of charge. We thank two anonymous reviewers and the editor (Kelly Russell) for comments that helped improve this manuscript.

References

Allard, P., Behncke, B., D'Amico, S., Neri, M., Gambino, S., 2006. Mount Etna 1993–2005: anatomy of an evolving eruptive cycle. Earth Sci. Rev. 78 (1–2), 85–114.
ASTM D4404-10, 2010. Standard Test Method for Determination of Pore Volume and Pore Volume Distribution of Soil and Rock by Mercury Intrusion Porosimetry. ASTM International, West Conshohocken, PA www.astm.org.
Barberi, F., Bertagnini, A., Landi, P., Principe, C., 1992. A review on phreatic eruptions and their precursors. J. Volcanol. Geotherm. Res. 52 (4), 231–246.
Behnsen, J., Faulkner, D.R., 2011. Water and argon permeability of phyllosilicate powders under medium to high pressure. J. Geophys. Res. Solid Earth 116 (B12).
Blower, J., 2001. Factors controlling permeability-porosity relationships in magma. Bull. Volcanol. 63 (7), 497–504.
Brace, W., Walsh, J.B., Frangos, W.T., 1968. Permeability of granite under high pressure. J. Geophys. Res. 73 (6), 2225–2236.
Brunauer, S., Emmett, P.H., Teller, E., 1938. Adsorption of gases in multimolecular layers. J. Am. Chem. Soc. 60 (2), 309–319.
Burgisser, A., Chevalier, L., Gardner, J.E., Castro, J.M., 2017. The percolation threshold and permeability evolution of ascending magmas. Earth Planet. Sci. Lett. 470, 37–47.
Byrdina, S., Vandemeulebrouck, J., Cardellini, C., Legaz, A., Camerlynck, C., Chiodini, G., ... Carrier, A., 2014. Relations between electrical resistivity, carbon dioxide flux, and self-potential in the shallow hydrothermal system of Solfatara (Phlegrean Fields, Italy). J. Volcanol. Geotherm. Res. 283, 172–182.

Chevalier, L., Collombet, M., Pinel, V., 2017. Temporal evolution of magma flow and degassing conditions during dome growth, insights from 2D numerical modeling. J. Volcanol. Geotherm. Res. 333, 116–133.

Chiodini, G., Allard, P., Caliro, S., Parello, F., 2000. ^{18}O exchange between steam and carbon dioxide in volcanic and hydrothermal gases: implications for the source of water. Geochim. Cosmochim. Acta 64 (14), 2479–2488.

Civan, F., 2010. Effective correlation of apparent gas permeability in tight porous media. Transp. Porous Media 82 (2), 375–384.

Collinson, A.S.D., Neuberg, J.W., 2012. Gas storage, transport and pressure changes in an evolving permeable volcanic edifice. J. Volcanol. Geotherm. Res. 243, 1–13.

Collombet, M., 2009. Two-dimensional gas loss for silicic magma flows: toward more realistic numerical models. Geophys. J. Int. 177 (1), 309–318.

Colombier, M., Wadsworth, F.B., Gurioli, L., Scheu, B., Kueppers, U., Di Muro, A., Dingwell, D.B., 2017. The evolution of pore connectivity in volcanic rocks. Earth Planet. Sci. Lett. 462, 99–109.

Costa, A., 2006. Permeability-porosity relationship: a reexamination of the Kozeny-Carman equation based on a fractal pore-space geometry assumption. Geophys. Res. Lett. 33 (2).

Darcy, H., 1856. The Public Fountains of the City of Dijon. Dalmont, Paris. 647.

Darot, M., Reuschlé, T., 2000. Acoustic wave velocity and permeability evolution during pressure cycles on a thermally cracked granite. Int. J. Rock Mech. Min. Sci. 37 (7), 1019–1026.

David, C., Menéndez, B., Darot, M., 1999. Influence of stress-induced and thermal cracking on physical properties and microstructure of La Peyratte granite. Int. J. Rock Mech. Min. Sci. 36 (4), 433–448.

Davy, C.A., Skoczylas, F., Barnichon, J.D., Lebon, P., 2007. Permeability of macro-cracked argillite under confinement: gas and water testing. Phys. Chem. Earth, Parts A/B/C 32 (8), 667–680.

Degruyter, W., Burgisser, A., Bachmann, O., Malaspinas, O., 2010. Synchrotron X-ray microtomography and lattice Boltzmann simulations of gas flow through volcanic pumices. Geosphere 6 (5), 470–481.

Edmonds, M., Oppenheimer, C., Pyle, D.M., Herd, R.A., Thompson, G., 2003. SO_2 emissions from Soufrière Hills volcano and their relationship to conduit permeability, hydrothermal interaction and degassing regime. J. Volcanol. Geotherm. Res. 124 (1), 23–43.

Eichelberger, J.C., Carrigan, C.R., Westrich, H.R., Price, R.H., 1986. Non-explosive silicic volcanism. Nature 323 (6089), 598–602.

Farquharson, J., Heap, M.J., Varley, N.R., Baud, P., Reuschlé, T., 2015. Permeability and porosity relationships of edifice-forming andesites: a combined field and laboratory study. J. Volcanol. Geotherm. Res. 297, 52–68.

Farquharson, J.I., Heap, M.J., Lavallée, Y., Varley, N.R., Baud, P., 2016. Evidence for the development of permeability anisotropy in lava domes and volcanic conduits. J. Volcanol. Geotherm. Res. 323, 163–185.

Farquharson, J.I., Wadsworth, F.B., Heap, M.J., Baud, P., 2017. Time-dependent permeability evolution in compacting volcanic fracture systems and implications for gas overpressure. J. Volcanol. Geotherm. Res. 339, 81–97.

Faulkner, D.R., Rutter, E.H., 2000. Comparisons of water and argon permeability in natural clay-bearing fault gouge under high pressure at 20 °C. J. Geophys. Res. Solid Earth 105 (B7), 16415–16426.

Faulkner, D.R., Rutter, E.H., 2003. The effect of temperature, the nature of the pore fluid, and subyield differential stress on the permeability of phyllosilicate-rich fault gouge. J. Geophys. Res. Solid Earth 108 (B5).

Firouzi, M., Alnoaimi, K., Kovscek, A., Wilcox, J., 2014. Klinkenberg effect on predicting and measuring helium permeability in gas shales. Int. J. Coal Geol. 123, 62–68.

Forchheimer, P.H., 1901. Wasserbewegung durch boden. Zeitz. Ver. Duetch Ing. 45, 1782–1788.

Fortin, J., Stanchits, S., Vinciguerra, S., Guéguen, Y., 2011. Influence of thermal and mechanical cracks on permeability and elastic wave velocities in a basalt from Mt. Etna volcano subjected to elevated pressure. Tectonophysics 503 (1), 60–74.

Fournier, N., Chardot, L., 2012. Understanding volcano hydrothermal unrest from geodetic observations: insights from numerical modeling and application to White Island volcano, New Zealand. J. Geophys. Res. Solid Earth 117 (B11).

Gaunt, H.E., Sammonds, P.R., Meredith, P.G., Smith, R., Pallister, J.S., 2014. Pathways for degassing during the lava dome eruption of Mount St. Helens 2004–2008. Geology 42 (11), 947–950.

Giggenbach, W.F., Soto, R.C., 1992. Isotopic and chemical composition of water and steam discharges from volcanic-magmatic-hydrothermal systems of the Guanacaste Geothermal Province, Costa Rica. Appl. Geochem. 7 (4), 309–332.

Guéguen, Y., Palciauskas, V., 1994. Introduction to the Physics of Rocks. Princeton University Press.

Heap, M.J., Kennedy, B.M., 2016. Exploring the scale-dependent permeability of fractured andesite. Earth Planet. Sci. Lett. 447, 139–150.

Heap, M.J., Baud, P., Meredith, P.G., Vinciguerra, S., Bell, A.F., Main, I.G., 2011. Brittle creep in basalt and its application to time-dependent volcano deformation. Earth Planet. Sci. Lett. 307 (1), 71–82.

Heap, M.J., Lavallée, Y., Petrakova, L., Baud, P., Reuschlé, T., Varley, N.R., Dingwell, D.B., 2014a. Microstructural controls on the physical and mechanical properties of edifice-forming andesites at Volcán de Colima, Mexico. J. Geophys. Res. Solid Earth 119 (4), 2925–2963.

Heap, M.J., Baud, P., Meredith, P.G., Vinciguerra, S., Reuschlé, T., 2014b. The permeability and elastic moduli of tuff from Campi Flegrei, Italy: implications for ground deformation modelling. Solid Earth 5 (1), 25.

Heap, M.J., Farquharson, J.I., Baud, P., Lavallée, Y., Reuschlé, T., 2015. Fracture and compaction of andesite in a volcanic edifice. Bull. Volcanol. 77 (6), 55.

Heap, M.J., Russell, J.K., Kennedy, L.A., 2016. Mechanical behaviour of dacite from Mount St. Helens (USA): a link between porosity and lava dome extrusion mechanism (dome or spine)? J. Volcanol. Geotherm. Res. 328, 159–177.

Heap, M.J., Kennedy, B.M., Farquharson, J.I., Ashworth, J., Mayer, K., Letham-Brake, M., ... Siratovich, P., 2017. A multidisciplinary approach to quantify the permeability of the Whakaari/White Island volcanic hydrothermal system (Taupo Volcanic Zone, New Zealand). J. Volcanol. Geotherm. Res. 332, 88–108.

Heller, R., Vermylen, J., Zoback, M., 2014. Experimental investigation of matrix permeability of gas shales. AAPG Bull. 98 (5), 975–995.

Houghton, B.F., Nairn, I.A., 1991. The 1976–1982 Strombolian and phreatomagmatic eruptions of White Island, New Zealand: eruptive and depositional mechanisms at a 'wet' volcano. Bull. Volcanol. 54 (1), 25–49.

Hurwitz, S., Kipp, K.L., Ingebritsen, S.E., Reid, M.E., 2003. Groundwater flow, heat transport, and water table position within volcanic edifices: implications for volcanic processes in the Cascade Range. J. Geophys. Res. Solid Earth 108 (B12).

Kendrick, J.E., Lavallée, Y., Hess, K.U., Heap, M.J., Gaunt, H.E., Meredith, P.G., Dingwell, D.B., 2013. Tracking the permeable porous network during strain-dependent magmatic flow. J. Volcanol. Geotherm. Res. 260, 117–126.

Klinkenberg, L.J., 1941. The permeability of porous media to liquids and gases. Drilling and Production Practice. American Petroleum Institute.

Kolzenburg, S., Heap, M.J., Lavallée, Y., Russell, J.K., Meredith, P.G., Dingwell, D.B., 2012. Strength and permeability recovery of tuffisite-bearing andesite. Solid Earth 3 (2), 191.

Kushnir, A.R., Martel, C., Bourdier, J.L., Heap, M.J., Reuschlé, T., Erdmann, S., ... Cholik, N., 2016. Probing permeability and microstructure: unravelling the role of a low-permeability dome on the explosivity of Merapi (Indonesia). J. Volcanol. Geotherm. Res. 316, 56–71.

Kushnir, A.R., Martel, C., Champallier, R., Arbaret, L., 2017a. In situ confirmation of permeability development in shearing bubble-bearing melts and implications for volcanic outgassing. Earth Planet. Sci. Lett. 458, 315–326.

Kushnir, A.R.L., Martel, C., Champallier, R., Wadsworth, F.B., 2017b. Permeability evolution in variably glassy basaltic andesites measured under magmatic conditions. Geophys. Res. Lett. https://doi.org/10.1002/2017GL074042.

Lavallée, Y., Benson, P.M., Heap, M.J., Hess, K.U., Flaws, A., Schillinger, B., ... Dingwell, D.B., 2013. Reconstructing magma failure and the degassing network of dome-building eruptions. Geology 41 (4), 515–518.

Le Ravalec, M., Darot, M., Reuschlé, T., Guéguen, Y., 1996. Transport properties and microstructural characteristics of a thermally cracked mylonite. Pure Appl. Geophys. 146 (2), 207–227.

Letham, E.A., Bustin, R.M., 2016. Klinkenberg gas slippage measurements as a means for shale pore structure characterization. Geofluids 16 (2), 264–278.

Lindoo, A., Larsen, J.F., Cashman, K.V., Dunn, A.L., Neill, O.K., 2016. An experimental study of permeability development as a function of crystal-free melt viscosity. Earth Planet. Sci. Lett. 435, 45–54.

Luquot, L., Gouze, P., 2009. Experimental determination of porosity and permeability changes induced by injection of CO_2 into carbonate rocks. Chem. Geol. 265 (1), 148–159.

Mayer, K., Scheu, B., Gilg, H.A., Heap, M.J., Kennedy, B.M., Lavallée, Y., ... Dingwell, D.B., 2015. Experimental constraints on phreatic eruption processes at Whakaari (White Island volcano). J. Volcanol. Geotherm. Res. 302, 150–162.

Melnik, O., Barmin, A.A., Sparks, R.S.J., 2005. Dynamics of magma flow inside volcanic conduits with bubble overpressure buildup and gas loss through permeable magma. J. Volcanol. Geotherm. Res. 143 (1), 53–68.

Montanaro, C., Scheu, B., Mayer, K., Orsi, G., Moretti, R., Isaia, R., Dingwell, D.B., 2016. Experimental investigations on the explosivity of steam-driven eruptions: a case study of Solfatara volcano (Campi Flegrei). J. Geophys. Res. Solid Earth 121 (11), 7996–8014.

Mueller, S., Melnik, O., Spieler, O., Scheu, B., Dingwell, D.B., 2005. Permeability and degassing of dome lavas undergoing rapid decompression: an experimental determination. Bull. Volcanol. 67 (6), 526–538.

Mueller, S., Scheu, B., Spieler, O., Dingwell, D.B., 2008. Permeability control on magma fragmentation. Geology 36 (5), 399–402.

Nara, Y., Meredith, P.G., Yoneda, T., Kaneko, K., 2011. Influence of macro-fractures and micro-fractures on permeability and elastic wave velocities in basalt at elevated pressure. Tectonophysics 503 (1), 52–59.

Noiriel, C., Gouze, P., Bernard, D., 2004. Investigation of porosity and permeability effects from microstructure changes during limestone dissolution. Geophys. Res. Lett. 31 (24).

Pérez-Flores, P., Wang, G., Mitchell, T.M., Meredith, P.G., Nara, Y., Sarkar, V., Cembrano, J., 2017. The effect of offset on fracture permeability of rocks from the Southern Andes Volcanic Zone, Chile. J. Struct. Geol. 104, 142–158.

Reid, M.E., 2004. Massive collapse of volcano edifices triggered by hydrothermal pressurization. Geology 32 (5), 373–376.

Rust, A.C., Cashman, K.V., 2004. Permeability of vesicular silicic magma: inertial and hysteresis effects. Earth Planet. Sci. Lett. 228 (1), 93–107.

Saar, M.O., Manga, M., 1999. Permeability-porosity relationship in vesicular basalts. Geophys. Res. Lett. 26 (1), 111–114.

Scheidegger, A.E., 1974. The Physics of Flow Through Porous Media. University of Toronto Press, Toronto. ISBN: 978-0802018496.

Sparks, R.S.J., 1997. Causes and consequences of pressurisation in lava dome eruptions. Earth Planet. Sci. Lett. 150 (3–4), 177–189.

Stanchits, S., Vinciguerra, S., Dresen, G., 2006. Ultrasonic velocities, acoustic emission characteristics and crack damage of basalt and granite. Pure Appl. Geophys. 163 (5–6), 975–994.

Tanikawa, W., Shimamoto, T., 2006. Klinkenberg effect for gas permeability and its comparison to water permeability for porous sedimentary rocks. Hydrol. Earth Syst. Sci. Discuss. 3 (4), 1315–1338.

Tanikawa, W., Shimamoto, T., 2009. Comparison of Klinkenberg-corrected gas permeability and water permeability in sedimentary rocks. Int. J. Rock Mech. Min. Sci. 46 (2), 229–238.

Taran, Y., Fischer, T.P., Pokrovsky, B., Sano, Y., Armienta, M.A., Macias, J.L., 1998. Geochemistry of the volcano-hydrothermal system of El Chichón Volcano, Chiapas, Mexico. Bull. Volcanol. 59 (6), 436–449.

Varley, N., Komorowski, J.-C., 2018. Volcán de Colima: Managing the Threat. Springer-Verlag, Berlin Heidelberg ISBN 978-3-642-25910-4.

Vasseur, J., Wadsworth, F.B., 2017. Sphere models for pore geometry and fluid permeability in heterogeneous magmas. Bull. Volcanol. 79 (11), 77.

Vinciguerra, S., Trovato, C., Meredith, P.G., Benson, P.M., 2005. Relating seismic velocities, thermal cracking and permeability in Mt. Etna and Iceland basalts. Int. J. Rock Mech. Min. Sci. 42 (7), 900–910.

Wadsworth, F.B., Vasseur, J., Scheu, B., Kendrick, J.E., Lavallée, Y., Dingwell, D.B., 2016. Universal scaling of fluid permeability during volcanic welding and sediment diagenesis. Geology 44 (3), 219–222.

Wright, H.M., Cashman, K.V., Gottesfeld, E.H., Roberts, J.J., 2009. Pore structure of volcanic clasts: measurements of permeability and electrical conductivity. Earth Planet. Sci. Lett. 280 (1), 93–104.

Zhang, M., Takahashi, M., Morin, R.H., Esaki, T., 2000. Evaluation and Application of the Transient-Pulse Technique for Determining the Hydraulic Properties of Low-Permeability Rocks—Part 2: Experimental Application.

Zhu, W., Baud, P., Vinciguerra, S., Wong, T.F., 2016. Micromechanics of brittle faulting and cataclastic flow in Mount Etna basalt. J. Geophys. Res. Solid Earth 121 (6), 4268–4289.